Long-Term Cycling Stability of Sodium/Sodium Ion Cells Probed by In Situ Solid-State NMR Spectroscopy

Sonja Egert, Renuka Remesh, Agatha Clarissa Jusdi, Yushi Sugawara, Konstantin Schutjajew, Martin Oschatz, Gerd Buntkowsky,* and Torsten Gutmann*

Sodium-ion batteries are at the forefront of new, sustainable energy systems required for the global energy transition. ^{23}Na in situ solid-state nuclear magnetic resonance spectroscopy is capable of unraveling structures in working electrochemical cells during the charging and discharging processes. To evaluate its suitability for long-term studies, local sodium environments in sodium/sodium ion cells based on silicon carbonitride and hard carbon materials are tracked for up to 49 cycles (228.5 h). The formation of dendrites as well as the decay of a secondary metallic sodium species is observed, and local structures are analyzed up to the point of capacity degradation and cell failure. Initial points of cell breakdown are reflected in the NMR data by characteristic changes in signal intensities, whereas the degradation of the cells is reflected by a cease to periodic signal intensity fluctuations. Meanwhile, ex situ ^{23}Na NMR spectra of the deactivated cells reveal a complex range of environments for sodium ions.

1. Introduction

Efficient energy storage is a cornerstone of the global transition to renewable energy and the expansion of electromobility.[1–3] As global demand for batteries grows—projected to exceed 1 TWh from 2030 onwards[2,4–6]—researchers are challenged to develop systems with larger energy density, increased charging speeds, improved safety, longer life-times, and lower costs.[1,2] While Li-ion batteries (LIB) dominate the market, concerns about the long-term availability of lithium and the sustainable management of resources under these growing demands are intensifying.[2,6,7]

Sodium-ion batteries (NIB) offer a promising alternative due to the abundance and worldwide availability of sodium resources[8–10] as well as the compatibility with existing LIB production lines.[11] By 2040, NIB and other next-generation systems are expected to reach a market share of 23–40%.[11] However, the ineffective intercalation of sodium into graphite anodes compared to lithium, ascribed to the thermodynamic instability of sodium-graphite intercalation compounds resulting from the absence of Na—C bond covalency,[12] has caused a significant challenge to their commercialization.[13] In addition, the difference in radius between sodium and lithium ions causes differences in the stability of cathode oxides and their phase transition behavior, whereas the lower charge density of sodium cations compared to lithium cations affects the chemistry in the interface between the cathode and the liquid electrolyte.[14]

Hence, there is a need for novel materials to meet the demands of modern batteries. Understanding the structure-function relationships of these materials is essential for improving NIB performances.[6,15]

Advancing NIB technology requires tools that can probe complex and less conventional redox processes.[1] To unravel the mechanisms by which all the materials in the cell work together and analyze nonequilibrium states, in situ and in operando techniques are needed. Solid-state nuclear magnetic resonance (NMR) spectroscopy enables in-depth structural insights into the entirety of Na or Li species in a working cell, including amorphous phases which are inaccessible by XRD.[1,16] In addition, NMR spectroscopy is nondestructive, capable of illuminating processes in the electrolyte, separators, electrodes, or at interfaces during cell operation, and can be carried out at variable temperatures and pressures.[17,18] In situ NMR spectroscopy is increasingly applied to LIB and NIB,[19–22] but quadrupolar and paramagnetic line broadening as well as inhomogeneities of the magnetic susceptibility in the cell

S. Egert, R. Remesh, A. C. Jusdi, Y. Sugawara, G. Buntkowsky, T. Gutmann
Eduard Zintl Institute for Inorganic and Physical Chemistry
Technical University of Darmstadt
Peter-Grünberg-Straße 8, 64287 Darmstadt, Germany
E-mail: Gerd.Buntkowsky@chemie.tu-darmstadt.de
gutmann@chemie.tu-darmstadt.de

S. Egert
School of Chemistry
EaStCHEM and Centre of Magnetic Resonance
University of St Andrews
North Haugh, St Andrews KY16 9ST, UK

K. Schutjajew, M. Oschatz
Helmholtz Institute for Polymers in Energy Applications Jena (HIPOLE Jena)
Lessingstraße 12–14, 07743 Jena, Germany

K. Schutjajew, M. Oschatz
Institute for Technical Chemistry and Environmental Chemistry
Friedrich Schiller University Jena
Philosophenweg 8a, 07743 Jena, Germany

T. Gutmann
Department of Chemistry, Physical Chemistry
University Paderborn
Warburger Straße 100, 33098 Paderborn, Germany

Batteries & Supercaps

Research Article
doi.org/10.1002/batt.202500516

Chemistry Europe
European Chemical
Societies Publishing

component complicate the interpretation of the resulting broad, overlapping spectral line shapes.[16,18,23,24] However, novel approaches for high resolution in situ NMR spectroscopy[25] and the analysis of in situ NMR data[26,27] have been proposed.

Typical in situ NMR setups use plastic (e.g., polyether ether ketone, PEEK) casings to ensure radiofrequency (RF) field penetration into the cell compartments,[13,17,28] though recent studies have begun exploring metal-cased cells.[29] However, the layout of the NMR spectrometer probe and RF coil pose limitations on the size, geometry, and materials that can be used.[22,30–34] While in situ ^{23}Na NMR spectroscopy can track structural changes and processes during the operation of the cell, its utility in long-term degradation studies remains underexplored, particularly compared to ^{7}Li NMR spectroscopy.[35,36]

This study tests the long-term stability of in situ PEEK cell capsules during extended cycling (up to 228.5 h and 49 cycles) using two electrode materials: silicon carbonitride (SiCN) and hard carbon (HC). Previous ^{23}Na in situ NMR studies of NIB materials have been typically focused on the structural changes during the initial charge and discharge cycles and have been limited to ≤2 cycles.[24,28,34,37–39] Here, we track sodium environments across multiple cycles, identifying key structural features.

Silicon-based polymer-derived ceramics (PDC) such as silicon carbonitride (SiCN)[40] are promising anode materials for LIB,[41–44] recently shown to reversibly store sodium under in situ conditions.[37] In this material, Si atoms are coordinated to C and N atoms in an amorphous covalent framework, forming a nanodomain structure.[45,46] Structural defects, graphene layer edges, and pores provide sites for ion adsorption and metal intercalation.[47–50]

Hard carbon (HC) materials—low-cost,[51] nongraphitizable carbons—are considered the most promising[52,53] and most widely used[15,27] anode materials for NIB. They are usually produced by pyrolysis of a duroplastic organic compound or biomass precursor[53] from a variety of sources including cotton textiles,[54] waste biomass,[52] or cellulose.[55] While the choice of precursor informs the electrochemical properties,[56] high storage capacities and high cycling stabilities have been reported.[52,53,57] The microcrystalline, defect-rich structures of HC feature nanopores[15,53] which can either be open, i.e. accessible to gas molecules, or closed, i.e. undetectable by gas physisorption.[52,58–60] Closed pores have been shown to stabilize quasimetallic sodium clusters at low and constant potentials against Na$^+$/Na, boosting the energy density, but tailoring the pore structure via precursor choice, additives, or post-synthetic coating (e.g., with polymeric carbon nitride, p-C$_3$N$_4$) remains challenging.[59] Sodium storage has been reported to be complex, consisting of combination of various processes.[27,61]

The reproducibility of electrochemical cell performance has recently been shown to be highly sensitive to variations of the assembly process.[62] To ensure consistency and assess the robustness of our methods, we assembled four cells with different working electrode materials and characterized them under identical conditions. This approach enabled us to evaluate overarching trends across different materials. Furthermore, the long-term cycling stability of the SiCN-based cell can be directly compared to data from previously reported in-depth studies.[37,63,64]

We analyze the local structures in Na/Na$^+$ PEEK cell capsules with SiCN and three different HC materials produced with different pore structures, identifying dendrite formation, the decay of a secondary sodium species, and structural changes during capacity degradation. To our knowledge, this work presents the first in situ ^{23}Na NMR study tracking the local structural evolution in NIB in-depth over the course of 8–48 cycles. By correlating NMR data with electrochemical performance, we demonstrate the viability of in situ NMR spectroscopy for long-term studies of cycling stability and degradation of electrochemical cells.

2. Results and Discussion

2.1. Long-Term Stability of SiCN Electrodes

Previous ^{23}Na in situ NMR studies[37] on PDC SiCN ceramics have demonstrated that these composite materials are suitable for sodium storage and an attractive option for electrode materials in Na-ion batteries, reporting the evolution of the local sodium environments over the course of 18 h, or two full cycles, as well as for up to 52 h monitoring the sodiation process. It was found that during the cycling, residual sodium deposition takes place, leading to the formation of 'dead' sodium without an electrical connection to the main electrode body.[37] In this work, the same material is cycled over a time period of 166 h, amounting to a total of nine full cycles. Meanwhile, ^{23}Na in situ data is continuously recorded to probe structural changes during prolonged use of the electrochemical cells and to determine whether similar or distinct changes occur as the cycling duration is increased.

The voltage profile and the capacity over time of the electrochemical cycling experiment are depicted in **Figure 1**a,b. The Na| NaPF$_6$|SiCN cell was continuously cycled nine times. The maximum capacity reached after the formation/plating process was approximately 75 mAhg^{-1} of which 24 mAhg^{-1} could be cycled reversibly, degrading over time to 12 mAhg^{-1}.

This is significantly lower than the capacity measured ex situ in Swagelok-type cells, where analogous materials achieved insertion capacities of up to 350 mAhg^{-1}.[63,64] We ascribe these differences to the variability of electrochemical performance depending on the assembly,[62] as well as differences in pressure and air-tightness across cell types. Figure S3, Supporting Information, shows a comparison of two cells prepared under identical conditions in a repeat experiment, indicating the variability in capacity and life-time that can arise as a result of the assembly.

However, most importantly, the shape of the sodiation curve in in situ experiments is similar to the one measured in Swagelok-type cells, pointing at the fact that the discrepancy is due to the incomplete utilization of active material in the NMR-setup rather than due to overpotentials.[37] Capacity fade over time is expected due to processes such as electrolyte decomposition, oxygen ingress into the cell, irreversible reactions, or contact loss.[65–67]

Figure 1c,d show the enlarged 3D view of the ^{23}Na in situ NMR spectra of the spectral regions corresponding to metallic sodium (1150 to 1080 ppm) and Na$^+$ ions in the electrolyte solution (20 to −50 ppm).[18,23,37] For the signal of Na$^+$ ions in the
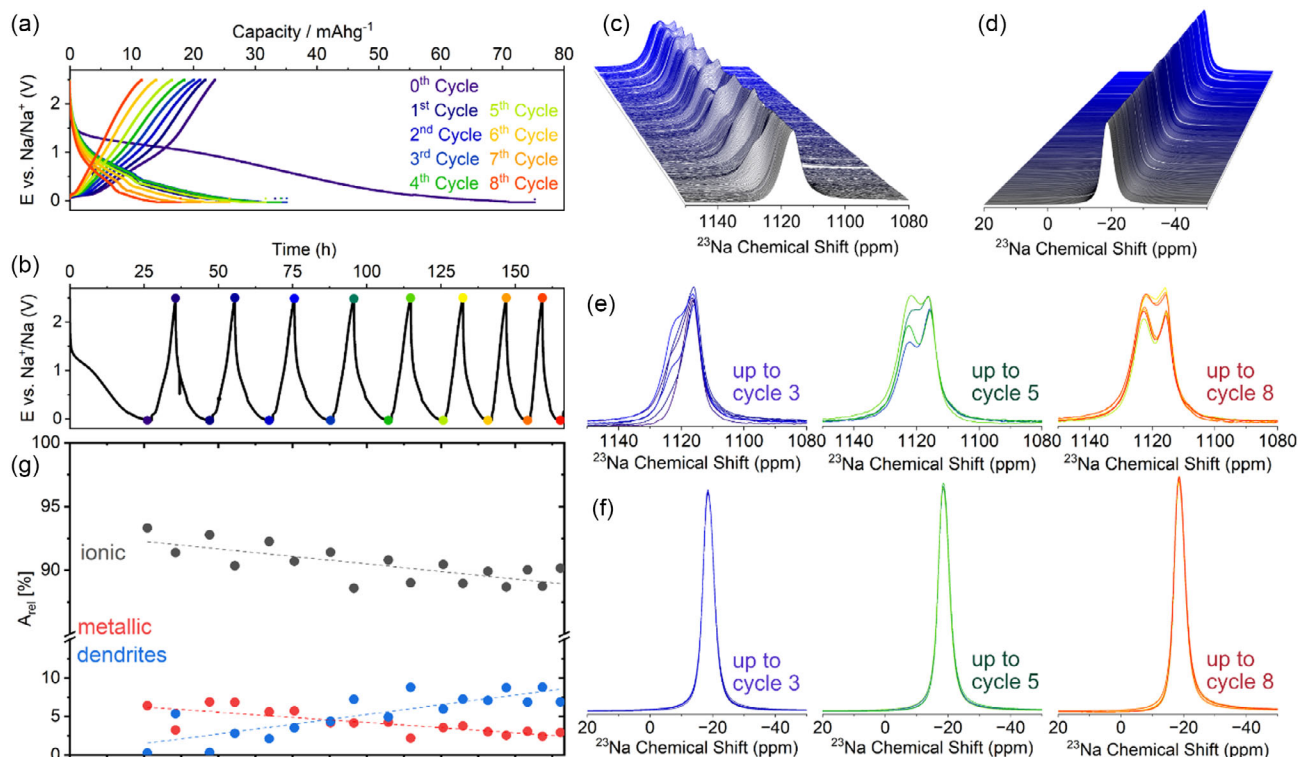
Figure 1. a) Capacity over time and b) voltage profile for the Na|NaPF$_6$|SiCN cell. The electrochemical cycling was conducted in the voltage window of −0.03 to 2.5 V vs. Na$^+$/Na applying a current of 20 µA for 166 h. Colored dots in the voltage profile mark the time stamps at which the ^{23}Na in situ NMR spectra in (f,g) were extracted. c,d) Enlarged 3D view of the ^{23}Na in situ NMR spectra of (c) the metal region, 1150 to 1080 ppm, and (d) the electrolyte region, 20 to −50 ppm. e,f) ^{23}Na in situ NMR spectra illustrating the fluctuations in intensity; blue: 0 to 87.8 h, green: up to 125.8 h, red: up to 165.2 h. A gradual growth of the signal corresponding to dendritic sodium at 1120 ppm is observed, with the relative peak area overtaking that metallic sodium signal at 1115 ppm from 87.8 h onwards. g) Relative peak areas A_{rel} of metallic sodium (1115 ppm), dendritic sodium (1120 ppm), and the signal of sodium in the electrolyte solution (−19 ppm) as obtained by peak deconvolution. Linear trend lines are added as a guide for the eye.

electrolyte solution at −19 ppm, slight fluctuations of the intensity are observed over the course of the cycling experiment which match the charge and discharge points. They are attributed to the formation of a solid–electrolyte interphase (SEI) at increasing voltages, while at decreasing voltages, sodium intercalation into the electrode occurs.[37,68] No signal corresponding to intercalated sodium species is observed, which has been attributed to insufficient resolution of signals broadened by quadrupolar and paramagnetic interactions.[37]

Meanwhile, for the signal assigned to metallic sodium at 1115 ppm, a significant change of the spectral line shape is observed, with an additional signal at −1120 ppm appearing during the first discharging cycle (voltages approaching 2.5 V). This signal, which appears as a shoulder during the early cycles, has previously been attributed to the growth of dendrites.[37] Over the course of the cycling experiment, the intensity of this signal fluctuates but do not return to its original state, indicating the formation of 'dead' sodium.[37] In the long-term cycling experiment carried out in the present work, it is observed that the intensity of this signal gradually overtakes that of the signal attributed to metallic sodium in the electrode.

These trends can be analyzed in a semi-quantitative manner by extracting ^{23}Na in situ spectra at defined stages of the cycling process and comparing the relative peak areas of the sodium ion

signal, the sodium metal signal, and the dendrite signal. Figure 1f,g show an overlay of seventeen ^{23}Na in situ NMR spectra extracted at the low- and high-voltage points of the cycling experiment (Figure 1b, colored dots) for both spectral regions. In the region from 20 to −50 ppm, a gradual decrease of the signal corresponding to ionic sodium species indicates continuous SEI formation over the course of the experiment. Meanwhile, in the region from 1150 to 1080 ppm, a gradual growth of the dendrite signal is observed during the initial sodiation from 12 h onwards as a shoulder. Fitting the overlapping lines with two Gaussian–Lorentzian functions yields the relative peak areas reported in Figure 1e. While all signal areas fluctuate according to the changing voltage, indicating a partially reversible process, a distinct increase of the dendrite signal is observed over time. Notably, its relative area overtakes that of the metallic signal from 87.8 h onwards.

Structure-wise, a continuation of the trends observed in the spectra recorded by Šić et al.[37] is observed. In their study, a signal attributed to the dendritic growth appeared after 8 h when the formation process was complete, manifesting as a signal shoulder and then increasing up to $A_{r,d} \approx 10\%$ during the second cycle, whereas the signal of metallic sodium decreased to $A_{r,m} \approx 14\%$ normalized to the entire spectral area. Hence, the dendritic signal amounted to approximately 40% of the metallic region.[37] In the present work, during the second cycle (E = 2.5 V), $A_{r,d} = 2.8\%$

Batteries & Supercaps

Research Article
doi.org/10.1002/batt.202500516

**Chemistry
Europe**
European Chemical
Societies Publishing

and $A_{r,m} = 6.8\%$, accounting for 29% of the metallic signal region. Meanwhile, during the eighth and final cycle (E = 2.5 V), $A_{r,d} = 8.8\%$ and $A_{r,m} = 2.4\%$, accounting for 78% of the metallic region.

Overall, the long-term study demonstrates the reproducibility of the previous work carried out by some of the authors[37] and robustness of the preparation of Na|NaPF$_6$|SiCN cells using the PEEK cell capsule setup typically used for in situ solid-state NMR studies. This highlights the suitability of solid-state NMR spectroscopy for studies of Na/Na$^+$ cells on a longer-term time scale, e.g., to probe the structural origins of cycling stability and capacity degradation.

2.2. Long-Term Stability of HC Electrodes

Having demonstrated the suitability of in situ solid-state NMR spectroscopy for studies of the long-term stability of model NIB, the approach is applied to a set of three different HC working electrodes. In HC materials, the electrochemical performance is affected by the choice of organic precursors[56] as well as the presence or absence of closed pores,[59] which act as hosts for quasimetallic sodium clusters during sodium storage.[24,38,39,59] In the present study, three different materials were used: **HC 1** is prepared via thermal treatment of cellulose, while during the synthesis of **HC 2**, p-C$_3$N$_4$ is employed as a pore-closing substance.[59] **HC 3**, a

commercially available Kynol, is intrinsically a closed-pore material. A comparison of the voltage profiles for all cells over the same time-scale is shown in Figure S2, Supporting Information.

2.2.1. HC 1

The prepared Na|NaPF6|**HC 1** cell was cycled for a total duration of 89.5 h during which the cell started to degrade after approximately 73.5 h or seven completed cycles (**Figure 2**a,b). The maximum capacity reached after plating was 145 mAhg^{-1}, of which 79 mAhg^{-1} could be reversibly cycled. At the end of the experiment, the discharge capacity had degraded to approximately 19 mAhg^{-1}. These values are substantially lower than those reported by Beda et al.[56] in ex situ experiments, probably due to the same reasons discussed for the SiCN-based cells.

Figure 2c,d show the ^{23}Na in situ NMR spectra of the metal and electrolyte region over the course of the cycling experiment. The initial growth and subsequent intensity changes of the dendrite signal (1120 ppm) following the applied voltage is observed. After 73.5 h, the intensity changes become minuscule, and the signal intensity no longer follows the applied voltage.

In comparison with a previous study on hard carbon powder electrodes Šić et al.,[34] the signal corresponding to metallic sodium in the **HC 1**-based cell is observed at 1115 ppm, shifted slightly
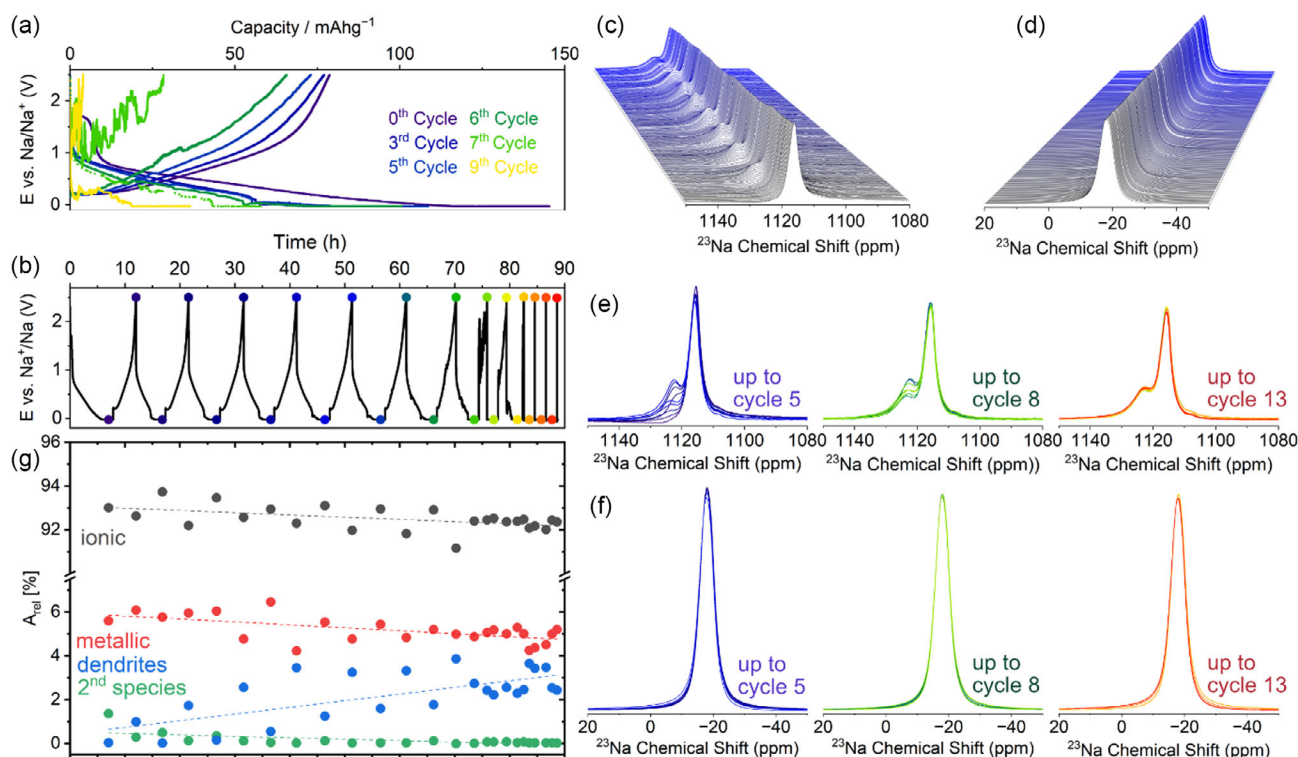

Figure 2. a) Capacity over time and b) voltage profile for the Na|NaPF$_6$|**HC 1** cell. Only selected cycles are depicted for clarity. Colored dots mark the time stamps at which the ^{23}Na in situ NMR spectra in (e,f) were extracted. c,d) Enlarged 3D view of the ^{23}Na in situ NMR spectra of (c) the metal region, 1150 to 1080 ppm, and (d) the electrolyte region, 20 to −50 ppm, of the Na|NaPF$_6$|HC 1 cell. e,f) ^{23}Na in situ NMR spectra illustrating the fluctuations in intensity; blue: 0 to 56.5 h, green: up to 75.9 h, red: up to 88.6 h. A gradual growth of the signal corresponding to dendritic sodium at 1120 ppm is observed, in addition to the decrease of a signal corresponding to a secondary sodium species at 1108 ppm. g) Relative peak areas A_{rel} of metallic sodium (1115 ppm), dendritic sodium (1120 ppm), and the signal of sodium in the electrolyte solution (−19 ppm) as obtained by peak deconvolution. Linear trend lines are added as a guide for the eye.

Batteries & Supercaps

Research Article
doi.org/10.1002/batt.202500516

Chemistry Europe
European Chemical
Societies Publishing

from the reported value of 1138 ppm. Notably, the signal shoulder corresponding to dendritic sodium appears at higher, rather than lower chemical shifts compared to the main metal signal (1120 ppm in our work vs 1132 ppm in the cited work). This may be related to the direction of dendrite growth due to the altered cell orientation, which is known to affect the chemical shift.[39] As shown in Figure 2e, the signal shoulder is well-resolved from the main signal, whereas for the powder-type electrode, the overlap is more pronounced.[34] Moreover, no significant variation in the position of the metallic sodium signal is observed in our setup, whereas in the powder cell configuration, a voltage-dependent shift of the signal maximum was reported.[34]

Overall, the signal position and line shape bear similarities to the SiCN-based cell, but the observed signal intensity of dendritic sodium does not increase as noticeably in the **HC 1**-based cell. However, a clear link between the degradation of the cell after 73.5 h and the NMR spectra is observed. As illustrated in Figure 2g, the beginning of the breakdown of the cell capacity at 73.5 h can be directly linked to a halt in the fluctuation of $A_{r,m}$ and $A_{r,d}$ alongside the variation of the voltage. As the capacity breaks down further after 83.6 h, the dendritic intensity increases abruptly. A halt of the increase or decrease of the dendrite and metal signals is consistent with the observations by Menkin et al. for in situ ^{7}Li NMR of lithium metal batteries;

however, they did not observe a corresponding abrupt increase of the dendrite signal intensity.[69]

The link between cell failure and intensity change demonstrates that in situ solid-state NMR measurements are suitable for tracking the origins of cell degradation in sodium-ion cells. Here, we observe a growth of dendrites and decrease of metallic sodium, culminating in both the metallic sodium and the dendritic sodium becoming inactive as the cell fails, directly reflecting the accumulation of 'dead' sodium.

Interestingly, in the **HC 1**-based cell in contrast to the SiCN-based cell, a secondary species is observed as a signal shoulder at 1108 ppm. This signal has the highest relative peak area of 1.35 % directly after plating; then, it immediately begins to decrease. It is tentatively proposed that the additional signal could originate from intermetallic sodium species, which have been reported[9,70] but not assigned to NMR signals.

2.2.2. HC 2

The Na|NaPF$_6$|**HC 2** cell was cycled for a total duration of 141 h during which the cell started to degrade after approximately 95.8 h or 20 completed cycles (**Figure 3**a). The capacity reached after plating was 44 mAhg^{-1}. Over the first 19 cycles, a fluctuation of the capacity is observed, with the value dropping to
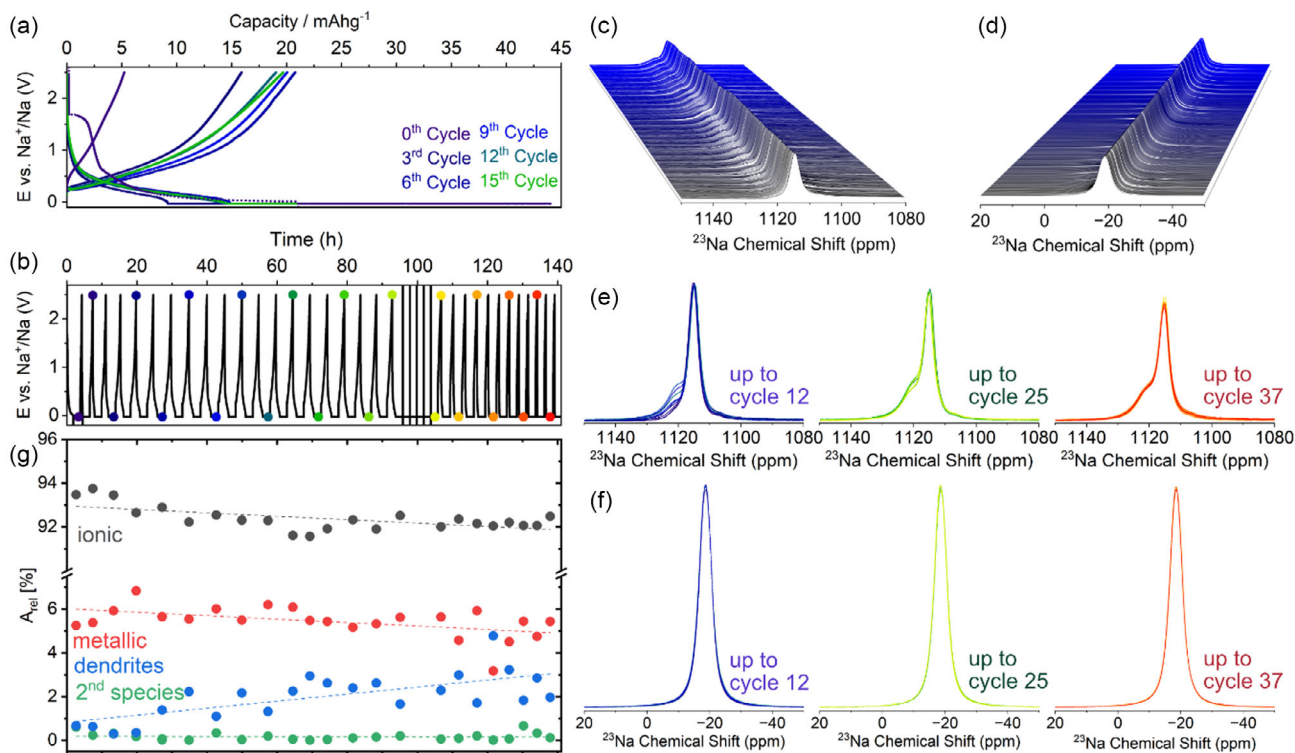

Figure 3. a) Capacity over time and b) voltage profile for the Na|NaPF$_6$|**HC 2** cell. Only selected cycles are depicted for clarity. Colored dots mark the time stamps at which the ^{23}Na in situ NMR spectra in (e,f) were extracted. c,d) Enlarged 3D view of the ^{23}Na in situ NMR spectra of (c) the metal region, 1150 to 1080 ppm, and (d) the electrolyte region, 20 to −50 ppm, of the Na|NaPF$_6$|**HC 2** cell. e,f) ^{23}Na in situ NMR spectra illustrating the fluctuations in intensity; blue: 0 to 57.4 h, green: up to 95.1 h, red: up to 137.9 h. A gradual growth of the signal corresponding to dendritic sodium at 1121 ppm is initially observed, but after around 94.5 h the fluctuations of this signal are decreased. An initially observed signal corresponding to a secondary sodium species at 1108 ppm decreases in intensity. g) Relative peak areas A_{rel} of metallic sodium (1115 ppm), dendritic sodium (1121 ppm), the secondary metallic species (1107 ppm), and the signal of sodium in the electrolyte solution (−19 ppm) as obtained by peak deconvolution. Linear trend lines are added as a guide for the eye.

Batteries & Supercaps

Research Article
doi.org/10.1002/batt.202500516

Chemistry Europe
European Chemical
Societies Publishing

$21\ \mathrm{mAhg^{-1}}$ during the third cycle, then increasing again up to $28\ \mathrm{mAhg^{-1}}$ during the sixth cycle. A gradual capacity degradation is followed by another increase from $22\ \mathrm{mAhg^{-1}}$ in the 13th cycle to $24\ \mathrm{mAhg^{-1}}$ in the 14th cycle, showing the same trend relative to Swagelok-type reference cells[59] as SiCN and **HC1**. We ascribe this fluctuation to the wetting and penetration of the electrode with sodium, which reduces overpotentials and allows for more capacity to be used up to the end-of-charge voltage. At the end of the experiment, the discharge capacity had degraded to approximately $10\ \mathrm{mAhg^{-1}}$.

Figure 3c,d show the ^{23}Na in situ NMR spectra of the metal and electrolyte region over the course of the cycling experiment, while Figure 3g depicts the evolution of the signal areas over time. Due to the length of the experiment, over the course of which the signal phases changed significantly, it was necessary to individually phase-correct the spectra extracted at the points of interest (Figure 3b) to ensure a reliable fitting procedure. Changes of the signal phase may be attributed to changes in conductivity.[38]

Qualitatively similar trends are observed as described for the **HC 1** cell, with a dendrite signal growing in intensity as the capacity degrades, and a secondary metallic species observed shortly after plating. However, even at the maximum relative intensity reached, the dendrite signal in the **HC 2** cell is less pronounced

than in the **HC 1** cell, potentially indicating differences in either the rate of growth or the shape of the dendrites formed. It is important to note, however, that due to variations in cell capacity and the duration of the cycling experiments, no definitive conclusions can be drawn regarding the structural origins of the observed differences in line shape.

2.2.3. HC 3

The Na|NaPF$_6$|**HC 3** cell was cycled for a total duration of 228.5 h and over 48 cycles (**Figure 4**a). The maximum capacity reached after plating was $32\ \mathrm{mAhg^{-1}}$. At the end of the experiment, the capacity on discharge had degraded to approximately $21\ \mathrm{mAhg^{-1}}$, similar to previously tested materials.[59] In contrast to the other cells, the **HC 3**-based cell was still reversibly cycling by the time the experiment was terminated.

Over the course of the cycling experiment, a steady increase of the dendrite signal was observed in the metallic region (Figure 4c), with the dendrite signal area matching that of the electrode signal area after approximately 108 h (Figure 4e). Only three species were considered for the **HC 3** cell due to the very low intensity in the region of the secondary sodium species. The intensities of the ionic, metallic, and dendritic signals continue to fluctuate until the termination of the NMR
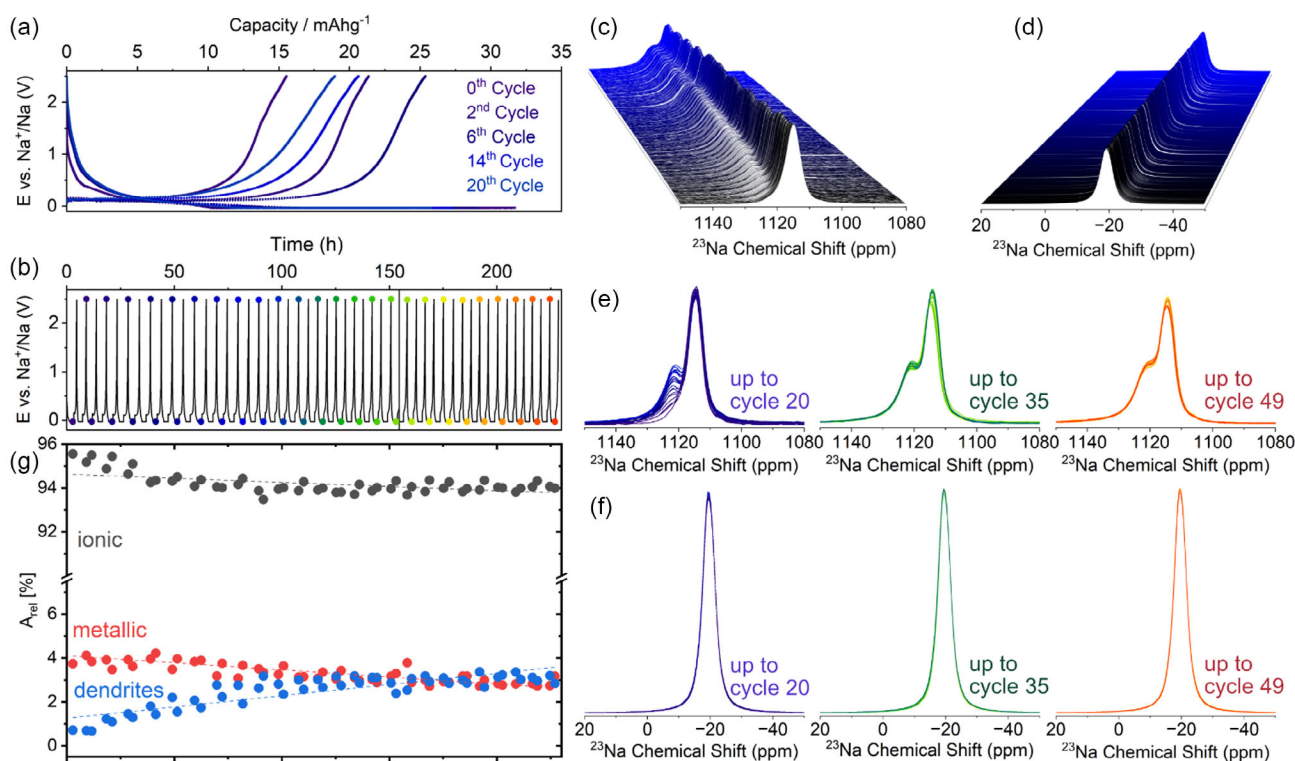

Figure 4. a) Capacity over time and b) voltage profile for the Na|NaPF$_6$|**HC 3** cell. Only selected cycles are depicted for clarity. Colored dots mark the time stamps at which the ^{23}Na in situ NMR spectra in (e,f) were extracted. c,d) Enlarged 3D view of the ^{23}Na in situ NMR spectra of (c) the metal region, 1150 to 1080 ppm, and (d) the electrolyte region, 20 to −50 ppm, of the Na|NaPF6|HC 2 cell. e,f) ^{23}Na in situ NMR spectra illustrating the fluctuations in intensity; blue: 0 to 100.8 h, green: up to 175.2 h, red: up to 226.9 h. A gradual growth of the signal corresponding to dendritic sodium at 1122 ppm is initially observed. The secondary sodium species was not considered in the deconvolution due to the very low intensity. g) Relative peak areas A_{rel} of metallic sodium (1115 ppm), dendritic sodium (1122 ppm), and the signal of sodium in the electrolyte solution (−19 ppm) as obtained by peak deconvolution. Linear trend lines are added as a guide for the eye.

measurement. The success of this cell demonstrates that up to 48 cycles, there are no hardware limitations for designing and carrying out long-term measurements with cell layouts used in in situ NMR spectroscopy.

2.3. Ex Situ Analysis of SiCN and HC Electrodes

To obtain higher-resolution ^{23}Na NMR spectra than the line broadening in the in situ setup allows, all cells were disassembled after galvanostatic cycling and the SiCN or HC materials were examined ex situ under magic angle spinning (MAS) conditions and at higher magnetic field. The resulting ^{23}Na NMR spectra are overlayed in **Figure 5**, normalized by the retrieved electrode mass and number of scans. No additional resonances are observed outside the chemical shift range depicted, indicating the absence—or intensity below the NMR detection limit—of signals corresponding to metallic sodium, expected above 1000 ppm, or quasimetallic clusters, expected between 1000 and 400 ppm.[39] This can either be attributed to the strong quadrupolar coupling and paramagnetic broadening of amorphous metallic species,[37] oxidation by traces of moisture and oxygen, amplified by heat generated during MAS,[34] or the generally degraded cell capacity at the end of the long-term experiments.

In the spectral region attributed to ionic sodium (50 to −50 ppm), several signals can be identified in the ex situ MAS spectra that overlap in the in situ data. In previous works, these signals are generally attributed to sodium ions in the electrolyte, in the SEI, intercalated between layers or stored in pores, and in decomposed sodium compounds.[71,72]

Signals appearing around 5 to 9 ppm can be attributed to the irreversible formation of sodium fluoride on the surface of the electrodes due to decomposition of the electrolyte.[34,37,73] This assignment is based on the comparison of both ^{19}F and ^{23}Na spectra of neat NaF carried out in previous studies.[37,73]

Residual electrolyte is typically observed as a sharp signal around −11 ppm[34,71] and was observed as an intense signal in our previous studies on SiCN and HC electrode materials.[34,37]

However, in the present study, overlapping signals of varying intensity are observed in this spectral region. This may be due to the cells having been cycled to failure, allowing for greater electrolyte evaporation than in previous ex situ NMR studies. The signal of the free electrolyte has been reported at −21 ppm,[34] and is not observed in the current study.

Broad signals in cycled HC materials centered around 12.8 and −7.5 ppm were previously assigned to sodium ions stored inside carbon layers and pores based on their large line widths indicating high disorder or restricted mobility.[34,71] Meanwhile, in cycled SiCN materials, a narrow signal at positive chemical shifts was assigned to sodium ions in symmetric environments, potentially close to the surface of the material,[37] whereas a broad signal at negative chemical shifts was assigned to either sodium carbonate species[37,73] or sodium ions in close vicinity to carbon layers and adsorbed on micropores.[37,68]

The assignment of signals observed in the ex situ NMR spectra is challenging due to their low resolution and signal-to-noise ratio, resulting in significant overlap. Unambiguous assignment of all species can be achieved using 2D techniques such as triple-quantum magic angle spinning (3QMAS) under fast MAS conditions at high magnetic fields. [73] This is outside of the scope of the present work due to the small amounts of cathode material recovered from the electrodes, ranging from 0.3 to 2.3 mg, and the necessity to carry out experiments directly after the end of the in situ experiments to avoid decomposition of species during the NMR experiment.[34]

In the spectra shown in Figure 5, signals above 10 ppm, tentatively assigned to stored sodium ions, show higher intensity for **HC 2** and **HC 3** than for **HC 1** and **SiCN**. Between 0 and −10 ppm, signals are observed for all materials, though their chemical shifts differ depending on the material, reflecting differences in local environments and sodium species present at the end of electrochemical cycling. These variations may arise from differences in cycling duration, recovered capacity, and the electrochemical state of the cells at the time of disassembly. Future studies should investigate how the choice of electrode material influences the observed end-of-life structures.

3. Conclusion

The suitability of in situ solid-state NMR spectroscopy for the long-term or life-cycle study of sodium-ion cells was examined for four novel electrode materials (SiCN, HC) over up to 49 cycles (228.5 h). It was demonstrated that long-term NMR measurements during galvanostatic cycling are accessible with PEEK cell capsules typically fabricated for in situ NMR probes. To our knowledge, the reported data presents the highest numbers of continuous galvanostatic cycles observed with in situ ^{23}Na NMR spectroscopy, closing the knowledge gap to ^{7}Li NMR spectroscopy.[35,36] It was shown that the ^{23}Na NMR data reflects the initial points of cell breakdown by characteristic changes in relative intensities, and the degradation of the cell as signal intensities cease to fluctuate periodically with the applied voltage consistently across four different materials. In addition, the
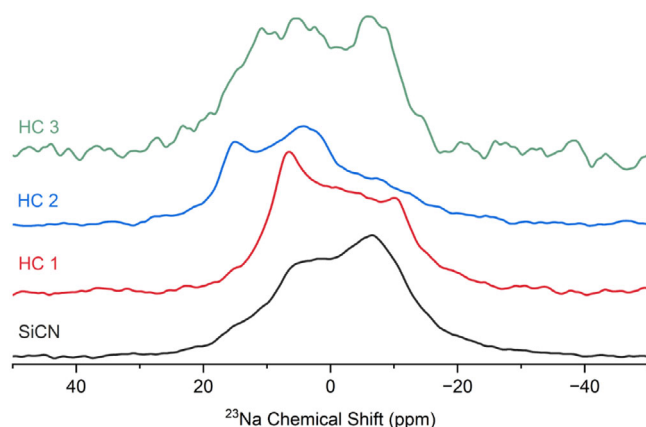

Figure 5. ^{23}Na ex situ MAS-NMR spectra at 10 kHz MAS of SiCN, **HC1**, **HC2**, and **HC3**, normalized with respect to the retrieved electrode mass and number of scans.

Batteries & Supercaps

Research Article
doi.org/10.1002/batt.202500516

Chemistry Europe
European Chemical
Societies Publishing

formation of dendrites and—in the case of two HC materials— the decay of a secondary metallic sodium species was observed over the course of the long cycling experiments. The ex situ NMR spectra showed a variety of environments for sodium ions intercalated or stored in structural cavities, probably due to differences of the material, the duration of galvanostatic cycling, the recovered capacity, and the state of the cell by the end of the experiment. Hence, they motivate further studies of the local environments of sodium species stored in the electrode materials, with a systematic variation in the number of electrochemical cycles. This will require the development of a more reproducible cell assembly process. Overall, the presented data is encouraging for the future use of NMR spectroscopy for tracking the origins of cell degradation and failure in NIB, contributing to the development of more sustainable battery alternatives with optimized lifetimes.

4. Experimental Section

Material Synthesis

Amorphous SiCN ceramics containing 40–50% carbon were produced from perhydropolysilazane dissolved in di-n-butyl ether (AZ Electronic Materials) and divinyl benzene (Sigma Aldrich) using Pt$^{(0)}$−1,3-divinyl-1,1,3,3-tetramethyldisiloxane (diluted in xylene; Sigma–Aldrich) as a catalyst. Reflux of the reaction mixture at 120 °C for 6 h enabled the hydrosilylation reaction to a preceramic intermediate. A crosslinking step at 250 °C (3 h) under argon atmosphere was followed by pyrolysis, heating at 100 °C/h to 1000 °C and holding for 3 h. After cooling the material at 100 °C/h to room temperature, the samples were ground and sieved to particle sizes < 40 μm. The procedure and resulting samples have previously been reported by Šić et al.[37] and Melzi d'Eril et al.[63,64]

HC 1 (Cellulose-1100) was synthesized following the method of Matei Ghimbeu et al.[74] Microcrystalline cellulose (Sigma Aldrich) was pyrolyzed in a horizontal tube furnace under inert conditions by first heating to 200 °C at a rate of 20 °C min^{-1}, followed by a subsequent heating to 450 °C at a rate of 1 °C min^{-1}. After cooling the sample to room temperature, it was subjected to a final heat treatment up to a temperature of 1100 °C at a heating rate of 3.3 °C min^{-1}. The sample was held at the final temperature for 1 h until it was cooled down to room temperature at natural cooling rate. **HC 2** was obtained by chemical vapor deposition (CVD) of polymeric carbon nitride p-C$_3$N$_4$ onto an activated carbon cloth (Kynol 5092-ACC10).[59] The commercially available carbon cloth was treated in an oxygen plasma using a plasma cleaner (Harrick PDC-32-G-2, 150 W power, 0.5 mbar pressure) for 10 min and immediately transferred into a tubular oven with two heating zones (planar-GROW-3S-OS CVD System for Organic Seminconductor, planarTECH, 3 in quartz tube) for CVD treatment. Five grams of melamine was placed upstream in the first zone with the target carbon cloth standing vertically downstream in the second zone. At a pressure of 10 Torr, melamine was fully sublimed at 300 °C and the deposition of p-C$_3$N$_4$ occurred at 550 °C in the target substrate zone. Nitrogen was used as a carrier gas at 50 sccm flow rate. The sample was cooled down naturally after completion of the process. For utilization of the material in electrodes, the cloth was ground down using a motorized mortar (Fritsch Pulverisette 2) in batches of 1 g for 10 min. **HC 3** is commercially available Kynol 5092-CC, ground analogously to **HC 2**.

Electrochemical Cell Setup and Cycling

Electrochemical cells (cylindrical, internal diameter of 15 mm, PEEK cell capsule OD15 short as provided by ePROBE[22,30,32] and schematic as previously reported[37]) were prepared under argon atmosphere keeping the water concentration below 0.5 ppm and the oxygen concentration below 4 ppm. Metallic sodium (Sigma-Alrich), serving as the counter and reference electrode, as well as the SiCN or HC working electrodes deposited on copper or aluminum foil, were connected to silver/copper current collectors and supported on 2-3 Teflon sheets to ensure dense packing of the cell components. Potentials are reported vs. Na$^+$/Na, if not stated otherwise. 2-3 borosilicate glass fiber sheets (Ahlstrom-Munksjö) served as separators and were saturated with 75 μL per sheet of 1 M NaPF$_6$ electrolyte in ethylene carbonate and diethyl carbonate (EC:DEC volume ratio of 3:7) with 5 wt.-% fluoroethylene carbonate additive (Xiamen Tob New Energy Technology Co., Ltd). The Na|NaPF$_6$|**HC 3** cell was reopened after initial cell failure and storage under inert conditions overnight to add further 75 μL of electrolyte. For the SiCN electrodes, two separator sheets were used, while the decreased thickness of the HC electrodes required three separators for dense packing. To ensure inert conditions within the cell and prevent sodium oxidation, the seams of the cell capsule were sealed with cyanoacrylate glue (Pattex) post assembly. The prepared cells were sodiated at a current of −20 μA until a voltage of −30 mV was reached, held for 2 h, and cycled applying a current of 20 μA, varying the voltage between −30 mV and 2.5 V vs Na$^+$/Na. All cells were cycled applying the same current. The specific capacities reported were scaled according to the active material loading as reported in the Supporting Information.

^{23}Na in Situ NMR Spectroscopy

^{23}Na in situ NMR measurements were performed on a Bruker Avance III spectrometer operating at 7.1 T, corresponding to a resonance frequency of 79.38 MHz for ^{23}Na. Assembled cells were connected to a single channel in situ probe (ePROBE), facilitating NMR spectroscopic measurements during galvanostatic cycling. In the probe geometry used in this work, electrochemical cells are oriented perpendicular with respect to the external magnetic field of the spectrometer. ^{23}Na NMR spectra were recorded using a pseudo-2D solid-echo sequence with an autotuning step after each increment, recalibrating the carrier frequency automatically by applying a low power continuous wave pulse (0.1 W) to optimize the tuning.[18] Low-pass filters were connected to the autotune controller to inhibit the passage of frequencies larger than 90 MHz. ^{23}Na chemical shifts were referenced to an external standard (signal of NaCl packed into a cell capsule at 0 ppm) according to ref. [75]. Echo pulse lengths were 5 μs at 300 W, recycle delays were 50 ms, and 15,000 transients were averaged in each single spectrum. 90° pulse lengths and short recycle delays[68] were chosen to maximize the signal-to-noise ratio, with the transmitter frequency offset set to the midpoint between the two observed resonances.

To evaluate the changes of signal components over time, each single spectrum was matched to a time stamp of the corresponding cycling experiment. A set of spectra was extracted, individually phase corrected, and deconvoluted by combined Gaussian and Lorentzian lines using MestreNova 14.0.0. No baseline correction was used; instead, the fit regions were restricted to the signal areas (−50 to 20 ppm and 1080 to 1150 ppm). Chemical shifts and line widths were allowed to vary freely during the fits. The fitting routine is described in more detail in the Supporting Information. As previously described by Šić et al.,[37] the areas of the signals corresponding to metallic sodium (1115 ppm, $A_{r,m}$),

Batteries & Supercaps

Research Article
doi.org/10.1002/batt.202500516

Chemistry Europe
European Chemical
Societies Publishing

dendritic sodium (1120 ppm, $A_{r,d}$), a secondary species (1107 ppm, $A_{r,s}$), and the signal of sodium ions in the electrolyte solution (-19 ppm, $A_{r,e}$) relative to the sum area ($A_{r,m} + A_{r,d} + A_{r,s} + A_{r,e}$) are then plotted as a function of time. It should be noted that the intensities are only semi-quantitative with respect to the sodium metal due to the occurring skin-depth effect.[76,77] We estimate the margin of error originating from variations in the phase correction, the baseline, and the fitting routine to be approximately 0.25% (see Supporting Information).

^{23}Na Ex Situ NMR Spectroscopy

After ending the cycling experiments, electrochemical cells were disassembled under argon atmosphere (water concentration below 0.5 ppm, oxygen concentration below 4 ppm). The working electrode material was scraped off the support foil and transferred into a 3.2 mm sapphire rotor with Teflon plug sealed with vespel caps. ^{23}Na ex situ NMR spectra were recorded on a Bruker Avance III spectrometer operating at 14.2 T, corresponding to a resonance frequency of 158.83 MHz for ^{23}Na. One-pulse experiments were performed at 10 kHz magic angle spinning (MAS) at an RF offset of 500 ppm and a short excitation pulse length of 0.2 μs, a recycle delay of 0.5 s, and a prescan delay of 10 μs. Short flip angles were used as they have been shown to result in uniform excitation in ex situ NMR spectra of NIB electrode materials;[37] meanwhile, the offset was set in between the chemical shifts expected for ionic and metallic sodium to ensure excitation across both spectral regions. Up to 84,000 transients were averaged.

Acknowledgements

Conflict of Interest

The authors declare no conflict of interest.

Data Availability Statement

The data that support the findings of this study are available from the corresponding author upon reasonable request.

[1] C. P. Grey, J. M. Tarascon, *Nat. Mater.* **2016**, *16*, 45.
[2] M. Fichtner, K. Edström, E. Ayerbe, M. Berecibar, A. Bhowmik, I. E. Castelli, S. Clark, R. Dominko, M. Erakca, A. A. Franco, A. Grimaud, *Adv. Energy Mater.* **2022**, *12*, 2102904.
[3] A. Manthiram, *Nat. Commun.* **2020**, *11*, 1550.
[4] A. Holland, X. He, *Batterien für stationäre Energiespeicherung 2021-2031* **2020**, can be found under https://www.idtechex.com/de/research-report/batteries-for-stationary-energy-storage-2021-2031/790 (accessed: April 2025).
[5] C. Nichols, *Batterien für stationäre Energiespeicher 2025-2035: Märkte, Prognosen, Akteure und Technologien* **2024**, can be found under https://www.idtechex.com/de/research-report/batteries-for-stationary-energy-storage-2025-2035-markets-forecasts-players-and-technologies/1021 (accessed: April 2025).
[6] C. P. Grey, D. S. Hall, *Nat. Commun.* **2020**, *11*, 6279.
[7] P. Greim, A. A. Solomon, C. Breyer, *Nat. Commun.* **2020**, *11*, 4570.
[8] K. B. Hueso, M. Armand, T. Rojo, *Energy Environ. Sci.* **2013**, *6*, 734.
[9] N. Yabuuchi, K. Kubota, M. Dahbi, S. Komaba, *Chem. Rev.* **2014**, *114*, 11636.
[10] B. Sun, P. Xiong, U. Maitra, D. Langsdorf, K. Yan, C. Wang, J. Janek, D. Schröder, G. Wang, *Adv. Mater.* **2020**, *32*, e1903891.
[11] J.-J. Marie, S. Gifford, *Faraday Insights* **2023**, *18*, 1.
[12] H. Moriwake, A. Kuwabara, C. A. J. Fisher, Y. Ikuhara, *RSC Adv.* **2017**, *7*, 36550.
[13] J. Chen, D. H. C. Chua, P. S. Lee, *Small Methods* **2020**, *4*, 1900648.
[14] Z.-Q. Lei, Y.-J. Guo, E.-H. Wang, W.-H. He, Y.-Y. Zhang, S. Xin, Y.-X. Yin, Y.-G. Guo, *Chem. Asian J.* **2022**, *17*, e202200213.
[15] Y. Chen, Z. Dong, S. Lai, Y. Li, W. Lv, Y.-B. He, F. Kang, M. Liu, *Adv. Funct. Mater.* **2024**, *34*, 2408657.
[16] K. Gotoh, T. Yamakami, I. Nishimura, H. Kometani, H. Ando, K. Hashi, T. Shimizu, H. Ishida, *J. Mater. Chem. A* **2020**, *8*, 14472.
[17] J. Z. Hu, N. R. Jaegers, M. Y. Hu, K. T. Mueller, *J. Phys. Condens. Matter* **2018**, *30*, 463001.
[18] O. Pecher, P. M. Bayley, H. Liu, Z. Liu, N. M. Trease, C. P. Grey, *J. Magn. Reson.* **2016**, *265*, 200.
[19] Y. Jiang, M. Zhao, Z. Peng, G. Zhong, *Magn. Reson. Lett.* **2024**, *4*, 200099.
[20] X. Liu, Z. Liang, Y. Xiang, M. Lin, Q. Li, Z. Liu, G. Zhong, R. Fu, Y. Yang, *Adv. Mater.* **2021**, *33*, 2005878.
[21] B. Z. Zheng, X. S. Liu, Y. X. Xiang, *J. Phys. Chem. C* **2024**, *128*, 18659.
[22] E. Šić, D. Fredericks, O. Pecher, S. Wegner, H. Breitke, V. Singh, G. Buntkowsky, T. Gutmann, *Appl. Magn. Reson.* **2024**, *55*, 575.
[23] P. M. Bayley, N. M. Trease, C. P. Grey, *J. Am. Chem. Soc.* **2016**, *138*, 1955.
[24] J. M. Stratford, P. K. Allan, O. Pecher, P. A. Chater, C. P. Grey, *Chem. Commun.* **2016**, *52*, 12430.
[25] I. Mohammad, M. A. Cambaz, A. Samoson, M. Fichtner, R. Witter, *Solid State Nucl. Magn. Reson.* **2024**, *129*, 101914.
[26] Y. Xiang, G. Zheng, Z. Liang, Y. Jin, X. Liu, S. Chen, K. Zhou, J. Zhu, M. Lin, H. He, J. Wan, *Nat. Nanotechnol.* **2020**, *15*, 883.
[27] J. M. Stratford, A. K. Kleppe, D. S. Keeble, P. A. Chater, S. S. Meysami, C. J. Wright, J. Barker, M.-M. Titirici, P. K. Allan, C. P. Grey, *J. Am. Chem. Soc.* **2021**, *143*, 14274.
[28] J. M. Bray, C. L. Doswell, G. E. Pavlovskaya, L. Chen, B. Kishore, H. Au, H. Alptekin, E. Kendrick, M.-M. Titirici, T. Meersmann, M. M. Britton, *Nat. Commun.* **2020**, *11*, 2083.
[29] B. J. Walder, M. S. Conradi, J. J. Borchardt, L. C. Merrill, E. G. Sorte, E. J. Deichmann, T. M. Anderson, T. M. Alam, K. L. Harrison, *Sci. Adv.* **2021**, *7*, eabg8298.
[30] O. Pecher, J. Carretero-González, K. J. Griffith, C. P. Grey, *Chem. Mater.* **2017**, *29*, 213.
[31] O. Pecher, A. Vyalikh, C. P. Grey, *AIP Conf. Proc.* **2016**, *1765*, 20011.
[32] O. Pecher, S. Wegner, *Battery Research Probes for Li-Ion Technologies (and Beyond)*, Application Note ePROBE GmbH and Bruker BioSpin GmbH, **2023**.
[33] F. Poli, J. S. Kshetrimayum, L. Monconduit, M. Letellier, *Electrochem. Commun.* **2011**, *13*, 1293.
[34] E. Šić, K. Schutjajew, U. Haagen, H. Breitke, M. Oschatz, G. Buntkowsky, T. Gutmann, *ChemSusChem* **2024**, *17*, e202301300.
[35] S. A. Kayser, A. Mester, A. Mertens, P. Jakes, R.-A. Eichel, J. Granwehr, *Phys. Chem. Chem. Phys.* **2018**, *20*, 13765.
[36] K. J. Sanders, A. A. Ciezki, A. Berno, I. C. Halalay, G. R. Goward, *J. Am. Chem. Soc.* **2023**, *145*, 21502.
[37] E. Šić, M. M. d'Eril, K. Schutjajew, M. J. Graczyk-Zajac, H. Breitke, R. Riedel, M. Oschatz, T. Gutmann, G. Buntkowsky, *Batteries Supercaps* **2022**, *5*, e202200066.
[38] A. Rajh, M. Gabrijelčič, B. Tratnik, K. Bučar, I. Arčon, M. Petric, R. Dominko, A. Vizintin, M. Kavčič, *Carbon* **2024**, *228*, 119398.
[39] M. Gabrijelčič, B. Tratnik, G. Kapun, E. Tchernychova, N. Z. Logar, A. Krajnc, R. Dominko, A. Vizintin, *J. Mater. Chem. A* **2025**, *13*, 1042.
[40] C. Gervais, *Open Ceram.* **2023**, *15*, 100376.
[41] S. Mukherjee, Z. Ren, G. Singh, *J. Phys. D: Appl. Phys.* **2018**, *51*, 463001.
[42] H. Fukui, H. Ohsuka, T. Hino, K. Kanamura, *ACS Appl. Mater. Interfaces* **2010**, *2*, 998.
[43] H. Fukui, H. Ohsuka, T. Hino, K. Kanamura, *J. Electrochem. Soc.* **2013**, *160*, A1276.
[44] M. S. Kolathodi, L. David, M. A. Abass, G. Singh, *RSC Adv.* **2016**, *6*, 74323.
[45] L. David, K. M. Shareef, M. A. Abass, G. Singh, *RSC Adv.* **2016**, *6*, 53894.

[46] D. Ahn, R. Raj, *J. Power Sources* **2011**, *196*, 2179.

[47] G. Mera, A. Navrotsky, S. Sen, H.-J. Kleebe, R. Riedel, *J. Mater. Chem. A* **2013**, *1*, 3826.

[48] E. Ionescu, H.-J. Kleebe, R. Riedel, *Chem. Soc. Rev.* **2012**, *41*, 5032.

[49] M. Li, L. Cheng, F. Ye, C. Zhang, J. Zhou, *J. Adv. Ceram.* **2021**, *10*, 1256.

[50] M. Graczyk-Zajac, L. M. Reinold, J. Kaspar, P. V. W. Sasikumar, G.-D. Soraru, R. Riedel, *Nanomaterials* **2015**, *5*, 233.

[51] X. Fan, X. Kong, P. Zhang, J. Wang, *Energy Storage Mater.* **2024**, *69*, 103386.

[52] X. Dou, I. Hasa, M. Hekmatfar, T. Diemant, R. J. Behm, D. Buchholz, S. Passerini, *ChemSusChem* **2017**, *10*, 2668.

[53] X. Dou, I. Hasa, D. Saurel, C. Vaalma, L. Wu, D. Buchholz, D. Bresser, S. Komaba, S. Passerini, *Mater. Today* **2019**, *23*, 87.

[54] H. R. Sarma, J. Sun, I. E. Gunathilaka, Y. Hora, M. Forsyth, N. Byrne, *SM& T* **2024**, *39*, e00846.

[55] V. Simone, A. Boulineau, A. de Geyer, D. Rouchon, L. Simonin, S. Martinet, *J. Energy Chem.* **2016**, *25*, 761.

[56] A. Beda, C. Villevieille, P.-L. Taberna, P. Simon, C. M. Ghimbeu, *J. Mater. Chem. A* **2020**, *8*, 5558.

[57] S. Komaba, W. Murata, T. Ishikawa, N. Yabuuchi, T. Ozeki, T. Nakayama, A. Ogata, K. Gotoh, K. Fujiwara, *Adv. Funct. Mater.* **2011**, *21*, 3859.

[58] K. Gotoh, T. Ishikawa, S. Shimadzu, N. Yabuuchi, S. Komaba, K. Takeda, A. Goto, K. Deguchi, S. Ohki, K. Hashi, T. Shimizu, *J. Power Sources* **2013**, *225*, 137.

[59] K. Schutjajew, P. Giusto, E. Härk, M. Oschatz, *Carbon* **2021**, *185*, 697.

[60] I. K. Ilic, K. Schutjajew, W. Zhang, M. Oschatz, *Carbon* **2022**, *186*, 55.

[61] H. Au, H. Alptekin, A. C. S. Jensen, E. Olsson, C. A. O'Keefe, T. Smith, M. Crespo-Ribadeneyra, T. F. Headen, C. P. Grey, Q. Cai, A. J. Drew, *Energy Environ. Sci.* **2020**, *13*, 3469.

[62] S. Puls, E. Nazmutdinova, F. Kalyk, H. M. Woolley, J. F. Thomsen, Z. Cheng, A. Fauchier-Magnan, A. Gautam, M. Gockeln, S.-Y. Ham, M. T. Hasan, *Nat. Energy* **2024**, *9*, 1310.

[63] M. M. d'Eril, M. J. Graczyk-Zajac, R. Riedel, *Batteries Supercaps* **2023**, *6*, e202200491.

[64] M. M. d'Eril, A. Kempf, D. M. de Carolis, M. J. Graczyk-Zajac, G. Mera, R. Riedel, *Batteries Supercaps* **2024**, *7*, e202400029.

[65] G. G. Eshetu, T. Diemant, M. Hekmatfar, S. Grugeon, R. J. Behm, S. Laruelle, M. Armand, S. Passerini, *Nano Energy* **2019**, *55*, 327.

[66] K. Du, C. Wang, L. U. Subasinghe, S. R. Gajella, M. Law, A. Rudola, P. Balaya, *Energy Storage Mater.* **2020**, *29*, 287.

[67] H. S. Hirsh, B. Sayahpour, A. Shen, W. Li, B. Lu, E. Zhao, M. Zhang, Y. S. Meng, *Energy Storage Mater.* **2021**, *42*, 78.

[68] K. Gotoh, *Batteries Supercaps* **2021**, *4*, 1267.

[69] S. Menkin, J. B. Fritzke, R. Larner, C. de Leeuw, Y. Choi, A. B. Gunnarsdóttir, C. P. Grey, *Faraday Discuss.* **2024**, *248*, 277.

[70] H. Morito, T. Yamada, T. Ikeda, H. Yamane, *J. Alloy Compd.* **2009**, *480*, 723.

[71] R. Morita, K. Gotoh, K. Kubota, S. Komaba, K. Hashi, T. Shimizu, H. Ishida, *Carbon* **2019**, *145*, 712.

[72] R. Morita, K. Gotoh, M. Fukunishi, K. Kubota, S. Komaba, N. Nishimura, T. Yumura, K. Deguchi, S. Ohki, T. Shimizu, H. Ishida, *J. Mater. Chem. A* **2016**, *4*, 13183.

[73] Z. E. M. Reeve, C. J. Franko, K. J. Harris, H. Yadegari, X. Sun, G. R. Goward, *J. Am. Chem. Soc.* **2017**, *139*, 595.

[74] C. M. Ghimbeu, J. Górka, V. Simone, L. Simonin, S. Martinet, C. Vix-Guterl, *Nano Energy* **2018**, *44*, 327.

[75] R. K. Harris, E. D. Becker, S. M. C. de Menezes, R. Goodfellow, P. Granger, *MRC* **2002**, *40*, 489.

[76] S. Chandrashekar, N. M. Trease, H. J. Chang, L.-S. Du, C. P. Grey, A. Jerschow, *Nat. Mater.* **2012**, *11*, 311.

[77] R. Bhattacharyya, B. Key, H. Chen, A. S. Best, A. F. Hollenkamp, C. P. Grey, *Nat. Mater.* **2010**, *9*, 504.